

Sample title

Eulerian CFD Model of Direct Absorption Solar Collector with NanofluidR. Bårdsgård,¹ D. M. Kuzmenkov,² P. Kosinski,^{1, a)} and B. V. Balakin^{3, b)}¹⁾University of Bergen, Department of Physics and Technology, Bergen, Norway²⁾National Research Nuclear University MEPhI, Moscow, Russia³⁾Western Norway University of Applied Sciences, Faculty of Engineering and Business Administration, Bergen, Norway

(Dated: 18 March 2020)

Solar energy is the most promising source of renewable energy. However, the solar energy harvesting process has relatively low efficiency, while the practical use of solar energy is challenging. Direct Absorption Solar Collectors (DASC) have been proved to be effective for a variety of applications. In this article, a numerical study of a nanofluid direct absorption solar collector was performed using CFD. A rectangular DASC with incident light on the top surface was simulated using a Eulerian-Eulerian two-phase model. The model was validated against experiments. A number of parameters such as collector height, particle concentration, and bottom surface properties were optimized. Considering particle concentration we observed that the optimum volume fraction of particles for enhancing efficiency was obtained for 0.3 wt%, and a decrease in efficiency was observed for ≥ 0.5 wt%. Design recommendations based on the numerical analysis were provided. The optimum configuration of the considered collector reaches the best efficiency of 68% for 300 μm thickness of the receiver and the highest total efficiency is 87% at a velocity of 3 cm/s. The thermal destabilization of the nanofluid was studied. It was found that over 10% of the nanoparticles are captured in the collector.

I. INTRODUCTION

Solar energy has the greatest potential among other sources of renewable energy when traditional energy sources are depleted¹. However, the electricity generation from solar energy is not efficient enough to replace fossil fuels and coal in northern countries, where solar resources are insufficient. In this case, the solar thermal power becomes more interesting, as over 65% of a household's electrical energy consumption is used to heat the premises². Enhancing the heat transfer process in solar energy systems is essential to achieving a better performance of these systems and reducing their dimensions. In a direct absorption solar collector (DASC), a semi-transparent heat transfer fluid absorbs the incident solar radiation volumetrically. This limits thermal leaks inherent for the traditional blackbody-based solar collectors.

Nanofluids are considered to be the most efficient heat transfer fluids for this type of collector. Otanicar et al.³ demonstrated four advantages of using DASCs over conventional collectors by studying how to improve the efficiency of nanofluid technology. These advantages include limiting heat losses from peak temperature, maximizing the spectral absorption of solar energy, enhancement of thermal conductivity, and enhancement of surface areas due to tiny particle sizes. They also studied a micro-sized DASC and observed a very promising enhancement of the collector's thermal efficiency relative to the flat-plate collector. Mirzaei et al.⁴ compared conventional flat-plate collectors and direct absorption solar collectors and observed an efficiency increase of 23.6% for nanoparticle (NP) volume fractions of 0.1%. The nanofluid used in their experiment was produced of 20-nm Al_2O_3 particles dispersed in water.

Recently, Neumann et al.⁵ have presented a detailed experimental description of photothermal heating of nanofluid exposed to thermal radiation. They studied several types of NPs dispersed in water and demonstrated efficient steam generation using solar illumination. The experiments were performed to study boiling by illumination and the resulting steam temperatures were over the boiling point of the base fluid. The thermodynamic analysis of the process showed that 80% of the absorbed sunlight was converted into water vapor, and only 20% of the absorbed light energy was converted into heating of the surrounding liquid. Ni et al.⁶ studied the effect of different nanofluids on the receiver efficiency by performing solar vapor generation experiments on a custom-built lab-scale receiver. In their study, for low concentration sunlight (10 suns), the efficiency was 69%. Running a numerical analysis of the problem, better performance was found in transient situations for graphitized CB and graphene nanofluids than for CB nanofluid. Finally, the study by Ghasemi et al.⁷ shows a solar thermal efficiency of up to 85% at low concentration sunlight.

Although there have not been many computational studies of the flow of nanofluids in DASC, a number of papers consider flow and heat transfer of nanofluids in thermal systems of other types. Yin et al.⁸ investigated the motion of aerosol NPs demonstrating that the main forces acting on the particle are the drag, Brownian and thermophoretic forces. The simulation results included the efficiency and deposition patterns at different temperature gradients. Haddad et al.⁹ observed that thermophoresis and Brownian motion enhanced heat transfer in the nanofluid. The enhancement was higher at lower volume fractions. Another study, by Burelbach et al.¹⁰, depicted the behavior of colloids under the impact of a thermophoretic force. They discovered that the thermophoretic force varies linearly with the temperature gradient.

A comprehensive numerical analysis of a micro-sized DASC with nanofluid was performed by Sharaf et al.¹¹, who modelled the collector using a Eulerian-Lagrangian approach.

^{a)}Electronic mail: pawel.kosinski@uib.no^{b)}Also at National Research Nuclear University MEPhI, Moscow, Russia

They discovered that the Reynolds number has a strong effect on the local NP distribution in the flow of nanofluid. The theoretical results obtained are important when designing this type of solar collector because they demonstrate how the performance of the collector depends on the spatial distribution of NPs. The simulation results were in excellent agreement with the experiment. However, the collector was modeled in two dimensions using the Lagrangian approach, demanding excessive computer power for a 3D-geometry due to a large number of particles. This method, therefore, becomes hardly scaled to a DASC with dimensions of industrial relevance. Another work by Sharaf et al.¹² investigated the geometry of micro-sized collectors. Their study indicated that lower collector heights give the best collector performance. Additionally, various surface materials were tested. Gorji and Ranjbar¹³ studied how to optimize the dimensions of a nanofluid-based DASC. They focused on the DASC geometry and its effect on thermal efficiency and entropy. Oppositely to Sharaf et al., one of the conclusions was that increased length and larger heights were beneficial for the desired parameters. Therefore, it may be concluded that there is no clear understanding of how the geometry of DASC influences the overall thermal performance of the collector.

A parametric analysis of a standalone nanofluid-based photothermal receiver was conducted in our previous works^{14–16}. The analysis was conducted using a two-fluid Eulerian-Eulerian multiphase CFD-model, which demands less computer power than the Lagrangian technique. The simulations were carried out for a three-dimensional geometry of the receiver considering how the composition of the nanofluid (concentration, particle size) and an external magnetic field influence the process. It was found that a nanofluid-based system has to be optimized in terms of both at the nanoscale (the position) and the macro-scale to set the receiver to the best efficiency point. However, the developed model did not consider the influence of the forced convection of the nanofluid. In addition, a simplified optical part of the model contributed to a 20% deviation from a benchmark experiment.

In this paper, we propose a pragmatic CFD-model of a NF-DASC based on the Eulerian-Eulerian approach. This approach requires low computational power and is, therefore, suitable for various particle concentrations and dimensions of the collector. The absorption of solar radiation was modeled using the theoretical approach by Bohren and Huffman¹⁷. Making use of the developed model, we studied how the boundary conditions, the dimensions of the collector and the flow velocity influence the thermal efficiency and deposition of nanoparticles in a microchannel-based solar collector.

II. MODEL DESCRIPTION

A. Flow geometry

The rectangular geometry modelled in this study was adapted from Otanicar et al.³, who constructed a micro-scale thermal-collector pumping nanofluid between two parallel plates with dimensions of $3 \times 5 \text{ cm}^2$. The thickness of the gap

was $150 \text{ }\mu\text{m}$. The experimental geometry is shown schematically in Fig. 1. The thermal stabilization of this system occurs after three minutes. Considering the fine meshing that is required for a system of a micrometric depth, the multiphase nature of the considered process, and the stabilization time, the CFD-model of a full-scale 3D DASC-NF demands large computational costs. To address this challenge, a conventional downscaling technique used previously in DASCs¹¹ and other multiphase systems¹⁸ was applied. A quasi-3D model of the collector was built. To reproduce the optical performance of DASC-NF, we used an equivalent depth of $150 \text{ }\mu\text{m}$. In addition, the equivalent residence time and incident thermal radiation were set with the length of the numerical model equal to 5 cm . This corresponded to the respective dimension along the main flow direction in the experiments. The thickness of the collector was equal to the size of four computational cells ($60 \text{ }\mu\text{m}$), and symmetry boundaries were set at the sides of the collector. The scaled model assumed minor variation of flow parameters in the direction orthogonal to the light-path and the main flow, which is a reasonable assumption for a fully developed flow with adiabatic thermal boundaries at the sides. The geometry was discretized with $20\text{-}\mu\text{m}$ uniform cubical mesh.

B. CFD-model

The nanofluid was modelled using the Eulerian-Eulerian two-fluid model, which assumes that both phases (base fluid and NPs) constitute two different interpenetrating fluids, with equal pressure. In this work, we used a standard Eulerian model of the commercial CFD-software STAR-CCM+. Conservation equations were assigned separately for each of the phases. The continuity equation is¹⁵:

$$\frac{D(\alpha_i \rho_i)}{Dt} = 0, \quad (1)$$

where D/Dt is the substantial derivative, and α_i , ρ_i and \mathbf{v}_i are the volume fraction, the density and the velocity vector of the respective phase. Each phase is denoted by $i = p$ for the NPs and $i = f$ for the base fluid, $\sum \alpha_i = 0$. The thermophysical properties of water were defined by IAWPS formulation¹⁹. The molecular properties of graphite were not available in the experimental article. Therefore, for this model we used the properties of graphite available from STAR-CCM+ database²⁰. The density of the particle material ρ_p was 2210 kg/m^3 .

The Eulerian momentum equation is given by¹⁵:

$$\frac{D(\alpha_i \rho_i \mathbf{v}_i)}{Dt} = -\alpha_i \nabla p + \nabla \cdot (\alpha_i \mu_i \nabla \mathbf{v}_i) + \alpha_i \rho_i \mathbf{g} + \mathbf{F}_D + \delta_{i,p} \mathbf{F}_{th}, \quad (2)$$

where p is the static pressure, μ is the dynamic viscosity, \mathbf{g} is the acceleration due to gravity and δ is Kronecker delta. The volume fraction of the particles in DASC is below 1%, so that the contribution of nanoparticles to the apparent viscosity of the nanofluid is assumed negligible. This is confirmed by the rheological study by Duan et al.²¹. Thus, we assumed

Sample title

3

particulate phase viscosity to be equivalent to the viscosity of the base fluid.

The drag force F_D is computed using the standard expression by Schiller-Naumann²² and further corrected with Cunningham's expression to account for rarefaction²²:

$$C_c = 1 + \text{Kn}(2.49 + 0.85\exp[-1.74/\text{Kn}]), \quad (3)$$

where Knudsen's number $\text{Kn} = \lambda_m/d_p$, $d_p = 30$ nm is the size of the particles and λ_m is the molecular mean free path in the base fluid.

Thermophoresis in dilute suspensions is driven by hydrodynamic stresses resulting from micro-scale interaction between particle and fluid¹⁰. The thermophoretic force F_{th} is computed following Brock's approximation²³:

$$F_{Th} = \frac{-6n_p\pi\mu_f\nu_fDC_s}{1+6C_m\text{Kn}} \frac{k_f/k_p+2C_l\text{Kn}}{1+2k_f/k_p+4C_l\text{Kn}} \nabla T, \quad (4)$$

where k_f is the thermal conductivity of phases, n_p is the number density of the particles, ν is the kinematic viscosity, C_s is the thermal slip coefficient, C_l is the thermal exchange coefficient, and C_m is the momentum exchange coefficient. The best values based on kinetic theory are $C_s = 1.17$, $C_l = 2.18$ and $C_m = 1.14$ ²². The thermal conductivity of the particles was 24 W/m·K.

The energy equation is given by²⁴:

$$\frac{D(\alpha_i\rho_i e_i)}{Dt} = \nabla(\alpha_i\rho_i\nabla T_i) - q_{ij} + \alpha_i q_v, \quad (5)$$

where $e_i = C_{pi}T_i$ is the phase-specific enthalpy, $C_{p,p} = 708$ J/kg·K, q_v is the volumetric heat generation due to absorption of radiant heat by the phases, and q_{ij} is the inter-phase heat transfer term. With the assumption that the convective heat transfer is established between the phases, the inter-phase heat transfer term is computed according to Ranz-Marshall²².

C. Optical model

The volumetric heat generation in nanofluid exposed to solar radiation was derived following Bohren and Huffman¹⁷ where the extinction cross-section of an individual spherical particle is:

$$C_{ext} = \frac{2\pi}{|x(\lambda)|^2} \sum_{i=1}^{\infty} (2i+1) \Re[a_i + b_i]. \quad (6)$$

In Eq. (6) λ is a wavelength, $x(\lambda) = 2\pi n(\lambda)/\lambda$ is a wave number; $n(\lambda)$ is a real part of the complex refractive index of the base fluid, and a_i and b_i are coefficients of scattered electromagnetic field, that can be written as follows:

$$a_i = \frac{m\psi_i(m\bar{\alpha})\psi'_i(\bar{\alpha}) - \psi_i(\bar{\alpha})\psi'_i(m\bar{\alpha})}{m\psi_i(m\bar{\alpha})\xi'_i(\alpha) - \xi_i(\bar{\alpha})\psi'_i(m\bar{\alpha})}; \quad (7)$$

$$b_i = \frac{\psi_i(m\bar{\alpha})\psi'_i(\bar{\alpha}) - m\psi_i(\bar{\alpha})\psi'_i(m\bar{\alpha})}{\psi_i(m\bar{\alpha})\xi'_i(\bar{\alpha}) - m\xi_i(\bar{\alpha})\psi'_i(m\bar{\alpha})}, \quad (8)$$

where m is a complex refractive index of the particle relative to the base fluid; $\bar{\alpha} = \pi n(\lambda)d_p/\lambda$ is the size parameter of particle; $\psi_i(z)$ and $\xi_i(z)$ are Riccati-Bessel functions of i -th order. Riccati-Bessel functions are related to the Bessel functions of the first (J_V) and second (Y_V) kind: $\psi_i(z) = \sqrt{\pi z/2}J_{i+1/2}(z)$ and $\xi_i(z) = \sqrt{\pi z/2}(J_{i+1/2}(z) + Y_{i+1/2}(z))$.

As can be seen from Eq.(6), the expression of the extinction cross-section includes infinite series that are hardly coupled with the multiphase CFD-model. In order to simplify this calculation, a maximum index n_{max} was used. According to Kiran and Diaz²⁵, a maximum index can be calculated as: $n_{max} = \lceil 2 + \bar{\alpha} + 4\bar{\alpha}^{1/3} \rceil$.

The extinction coefficient of particles in nanofluid with volume fraction α_p can be calculated according to Taylor et al.²⁶:

$$\sigma_p = \frac{3}{2} \alpha_p \frac{Q_{ext}}{d_p}, \quad (9)$$

where Q_{ext} is the extinction efficiency, which is related to the extinction cross-section, as $Q_{ext} = C_{ext}/S_p$, with S_p being the area of the particle cross-section.

The total extinction coefficient of the nanofluid is composed of particle and base fluid extinction coefficients:

$$\sigma_{nf} = \sigma_p + (1 - \alpha_p)\sigma_f, \quad (10)$$

where σ_f is the extinction coefficient of the continuous phase, which can be calculated according to Bohren and Huffman¹⁷ as $\sigma_f = 4\pi k(\lambda)/\lambda$; and $k(\lambda)$ is the imaginary part of the complex refractive index of the base fluid. The optical properties of the base fluid $k(\lambda)$ and the particles m are found elsewhere^{27,28}.

In order to calculate the solar heat flux in nanofluid as a function of distance from the exposed surface, it is necessary to specify the spectral distribution of incident radiation $I(\lambda)$, which is given in²⁹⁻³¹.

According to Beer-Lambert's law, the solar heat flux in nanofluid decays as follows:

$$q = \int_0^{\infty} I(\lambda) \exp[-x\sigma_{nf}] dx. \quad (11)$$

Eq. (11) is not applicable for use in CFD simulation due to the high computational costs associated with the integration of the function. To realize the calculation of solar heat flux in the model, the equivalent depth of optical penetration l_{eq} was computed for 30-nm carbon nanoparticles at different particle concentrations. The equivalent depth of optical penetration is defined as a distance from the light entrance to the nanofluid, towards the place at which the total heat flux becomes e times smaller. Thus, the equivalent depth of optical penetration is computed when the numerically-solved Eq.

Sample title

4

(11) becomes equivalent $q_0 e^{-1}$. The reciprocal of the equivalent depth of optical penetration, $\bar{\sigma}_{nf} = l_{eq}^{-1}$, is considered as the equivalent extinction coefficient.

Equation (11) was solved numerically in Wolfram Mathematica outside the CFD model for a variety of nanoparticle concentrations. The integral in Eq. (11) was computed using the trapezoidal rule with 1 nm wavelength steps. Further, we fitted the equivalent extinction coefficient as a function of particle volume fraction with a simplified expression of the type using the conjugate gradient method³²:

$$\bar{\sigma}_{nf} = \frac{2}{\pi} (A + B\alpha_p) \arctan(\kappa\alpha_p) + 0.58. \quad (12)$$

Fitting the equivalent extinction coefficient $\bar{\sigma}_{nf}$ with the expression from Eq. (12) resulted in the following values of fitting coefficients: $A = 2020.07 \text{ m}^{-1}$, $B = 9.53094 \cdot 10^6 \text{ m}^{-1}$ and $\kappa = 8031.63$. The approximation result is presented in Fig. 2, where the extinction coefficient is resolved numerically (line) and compared to Eq. (12) (boxes) for different particle concentrations.

The solar heat flux in nanofluid can be written as $q = q_0 \exp[-x\bar{\sigma}_{nf}]$, where $q_0 = 1$ sun is the incident solar radiation. The volumetric heat generation then becomes:

$$q_v = -dq/dx = q_0 \bar{\sigma}_{nf} \exp(-\bar{\sigma}_{nf} l), \quad (13)$$

where l is the optical path in the direction of thermal radiation

D. Boundary conditions and numerical solution

The boundary conditions include two symmetry planes at the frontal surfaces of the model, and a velocity inlet on the left of the studied section. The inlet velocity corresponded to the volume flow rate of 42 ml/h, as in the experiment³. The inlet boundary condition set the uniform distribution of velocity, volume fraction and temperature 25°C. The equivalent flow parameters were set for the initial condition. The outlet boundary defined the zero-field of relative pressure, uniform distribution of volume fraction and zero gradient of temperature.

The bottom and the top boundary were no-slip walls. The top wall of the DASC was exposed to solar radiation, and the distribution of volumetric heat generation was set accordingly to Eq. (13). Following Otanicar et al.³, the top boundary was identified as the only source of thermal loss with an equivalent heat transfer coefficient in the range $h \in [23, 34] \text{ W/m}^2\text{K}$ of the experimental range of nanoparticle concentrations. This coefficient accounted for thermal leaks due to convection of air around the collector and thermal radiation at the ambient temperature of 25°C.

There were two alternatives for the bottom boundary thermal condition. An adiabatic boundary was prescribed for the base-case simulations. Furthermore, to understand the influence of a black-body bottom of the collector, we prescribed a constant heat flux at this boundary. The absolute value of the boundary heat flux was set proportionally to the

radiant heat flux penetrating the nanofluid down to the bottom of the collector and further absorbed by the bottom.

Eqs. (1-5) were solved using the commercial CFD package STAR-CCM+ 13.06.012, running in parallel on eight cores of 2.5 GHz. The numerical solution was obtained using an implicit SIMPLE technique, and the following relaxation coefficients were applied: 0.3 for pressure, 0.7 for velocity, 0.5 for phase volume fraction, 0.9 for the enthalpy, and 0.8 for the turbulence model (see section III D). The governing equations were discretized temporally with the second-order Euler technique marching by 1.0 ms. The upwind scheme was applied for spatial discretization. Each simulation point was run for two-three periods of the system's thermal relaxation time until the residuals reduced below 10^{-6} and the system pressure drop converged at a steady-state value.

III. RESULTS AND DISCUSSION

A. Model validation

The model was validated against the experimental results from Otanicar et al.³. The model-predicted thermal efficiency of the collector was compared to the respective parameter determined experimentally. Following ASHRAE standard³³, this parameter is defined as a ratio of the collector-harvested heat to the incident heat. In this study, the harvested heat is defined according to Sharaf et al.¹¹ as the spatially-averaged rate of the enthalpy difference between the open ends of the collector:

$$\eta_T = \frac{\int_{y=0}^{y=H} (v_o C_{nf,o} \rho_{nf,o} T_{f,o} - v_i C_{nf,i} \rho_{nf,i} T_{f,i}) dy}{q_0 \cdot H}, \quad (14)$$

where H is the thickness of the collector in the direction normal to flow and solar radiation: $C_{nf} = \alpha_p C_{p,p} + \alpha_i C_{p,i}$ and $\rho_{nf} = \alpha_p \rho_p + \alpha_i \rho_i$ are the equivalent specific heat and the density of the nanofluid, and indices o and i denote inlet and outlet boundaries. The proposed method accounts for the spatial variation of the main flow parameters.

It is important to note that another expression for the harvested heat was used in the original work by Otanicar et al.³: $\dot{m} C_{p,f} (T_{f,o} - T_{f,i})$, where \dot{m} is the mass flow rate. In the case of the constant volumetric flow rate at the inlet, the latter parameter was dependent on the reference temperature of DASC, which might differ between the model and the experiment.

Validating our model in Fig. 3, we note a qualitatively similar evolution of the thermal efficiency at different particle concentrations. The DASC does not entirely absorb the radiant heat at a dilute particle concentration so that the efficiency is low there. Furthermore, when increasing the number of nanoparticles the efficiency goes up to 62% at 0.3 wt%. For even higher NP concentration, most of the radiant heat absorbs at the top surface of the collector, increasing the temperature of the top boundary. This enhances the thermal leak to the surroundings and the thermal efficiency of the collector

Sample title

5

is reduced again. The maximum discrepancy of the experiments is 12% and the greatest deviation from the experiment is observed close to the maximum of the function. This inaccuracy is addressed to the simplification that we made for the bottom boundary condition, which was reflective in the experiments. In addition, there is an experimental uncertainty in the determination of thermal leaks. Analyzing the infrared images of the experimental system (Fig. 1 of the original article³), we detect a very non-uniform temperature field in the most remote corners of the collector. Most probably, this is associated with the not entirely developed flow field, particle deposition, and the resulting local thermal leaks. These details are not reproduced in the model using the symmetry assumption we took, so that the experimental efficiency is expected to be lower than the theoretical. In addition, we note that the theoretical efficiency at high concentrations reduces steeper than in the experiment. This can be addressed to the fact that the model does not account for particle-wall collisions and thus the near-wall absorption is higher. This increases thermal leaks. The unknown reference temperature, the approximated extinction coefficient (Eq. 12), and a potential agglomeration of nanoparticles in liquid contribute to the discrepancy.

solar collector, we considered another parameter, termed the deposition efficiency, which is given as:

$$\eta_{dep} = \frac{\alpha_{p,in} - \alpha_{p,out}}{\alpha_{p,in}} \times 100\%, \quad (15)$$

where $\alpha_{p,in}$ and $\alpha_{p,out}$ are the volume fraction of particles at inlet and outlet.

Fig. 6a shows the results from these simulations for different collector sizes and types of boundary conditions. As the figure shows, the greatest deposition efficiency was 11% for the lowest size of the gap. Furthermore, increasing the size reduces the deposition efficiency. This is explained by the destabilizing action of the thermophoretic force, which deposits more particles in a narrow gap, while the disperse action of drag becomes stronger for a wider collector. Moreover, the temperature decreases with the height of the collector, weakening the thermophoresis. For the model with a black absorptive bottom surface, the deposition efficiency is higher. Fig. 6b shows that the deposition efficiency reduces asymptotically to 0.8% with the mean flow velocity, due to better agitation of the dispersed phase.

B. Flow asymmetry

C. Parametric analysis

Fig. 4a demonstrates profiles of the nanoparticle concentration at different axial positions of the collector. According to the figure nanoparticles are not uniformly distributed over the cross-section; the profiles are asymmetrical. This is explained by the mutual action of gravity and thermophoresis drifting the particles towards the bottom boundary. The asymmetry increases closer to the outlet from the collector. The deposition of particles influences the optical properties of the nanofluid. Our model results are shown in Fig. 4b confirm the simulations by¹¹, who first demonstrated a reduction of the extinction coefficient at the surfaces of the collector.

To highlight the development of flow patterns in the collector, Fig. 5 shows the particulate phase velocity and the temperature distribution in transverse cross-sections at 1 cm, 2 cm, 3 cm, and 4 cm from the inlet. In the figure, it is possible to note the development of convective flow patterns from the top of the collector at 2 cm and further from the bottom at 3 cm. The maximum magnitude of the secondary flow is below 7% of the main flow velocity. This means the secondary flow plays a minor role in transport of particles. The upper vortex is formed under the influence of the thermophoresis of particles, and the Rayleigh-Taylor structure at the bottom is caused by the sedimentation of particles and the respective up-rise of the base fluid. The distribution of temperature is very uniform in these cross-sections, even though it is possible to observe a gradual reduction of the temperature gradient due to the enhanced mixing of the flow. The insert at the bottom of the figure presents the axial distribution of the temperature profile. We notice that the temperature gradually increases in the axial direction until the profile stabilizes at 1.3 cm from the inlet.

In order to investigate how the nanoparticles deposit in the

The height of the solar collector has a vital influence on the amount of heat absorbed and transferred by the nanofluid. There is an optimum height/length ratio associated with the best thermal performance of the collector¹³. The results of the model-based optimization are presented in Fig. 7, where the thermal efficiency and the outlet temperature are shown for different heights of the collector and types of the bottom boundary. As the figure shows, by increasing the thickness less heat is taken by the nanofluid flow and the outlet temperature decreases. The outlet temperature decreases almost linearly with the collector height. This limits the thermal losses and the collector efficiency increases. The observed dependence of the thermal efficiency on the height of the volumetric receiver is consistent with the results obtained by¹². However, at a thickness of 300 μm , the efficiency begins to reduce as the volumetric absorption is no longer active across the entire volume of nanofluid. The consumed heat, therefore, is transferred to internal fluid layers with the incipient volumetric absorption, which reduces the thermal efficiency.

Fig. 7 shows that for collector heights lower than 200 μm , the efficiency is higher for the model with the black absorbing bottom plate. In this case, a warmer bottom surface returns absorbed heat back into the process, boosts the thermal efficiency, and increases the outlet temperature. At the point of maximum difference, the efficiency is 12% higher for the black bottom plate, than for the transmissible adiabatic plate. This occurs at the lowest collector height tested, 50 μm . For collector heights above 200 μm , the thermal efficiency decays towards the values for the case with the adiabatic bottom. This can be explained by the fact that on increasing the gap, the nanofluid consumes most of the thermal radiation in the bulk and the bottom does not receive sufficient heat.

Otanicar et al.³ considered an experimental case, where the bottom copper plate was painted black, to imitate an absorbing black-body, which resulted in increased collector efficiency. The blackbody absorbed the rest of the transmitted radiation and heated up the fluid so that the thermal convection developed from the bottom surface of the collector. The supplementary mixing in the direction transverse to the main flow boosted the thermal efficiency. We reproduced this experiment numerically for the case where only the continuous phase (water) was present in the collector. In addition, we performed another simulation, where the perfect absorption was assumed at the top boundary so that the heat flux equivalent to q_0 was prescribed there. The volumetric absorption results were obtained from the model with a volume fraction of particles at 0.3 wt% and a collector height of 300 μm . Fig. 8 shows the difference in efficiency for the different collectors. As the figure shows, the volumetric absorption system outperforms the surface-based collector by at least 20%. This result is consistent with our previous studies¹⁵.

D. Total efficiency

Studying the influence of flow rate on the thermal efficiency of the process, we note the pumping cost penalty growing with the flow velocity. To account for this effect, we define a total efficiency of the process:

$$\eta = \eta_T - \frac{Q\Delta P}{q_0 A}, \quad (16)$$

where Q is the volumetric flow, ΔP is the friction pressure drop in the collector, and A is the irradiated area of the collector. Another factor that needs to be accounted for is the turbulence that occurs when $v > 4.6$ cm/s. To calculate the turbulent stress in Eq. 2 of the continuous phase, the CFD-model was updated with $k - \epsilon$ turbulence model (standard wall functions). The turbulent viscosity of the particulate phase was set proportional to the turbulent viscosity of the base fluid. Fig. 9 demonstrates how the total efficiency and the pressure drop depend on the mean flow velocity.

The results from Fig. 9 show that a peak efficiency of 87% is obtained at $u=3$ cm/s. This efficiency is 42% higher than for the base case and 30% higher than the maximum efficiency obtained when optimizing the collector height. We also note that the pumping cost penalty in Fig. 9 increases continuously with the mean flow velocity so that the total efficiency decreases for velocities > 4 cm/s.

IV. CONCLUSION

A Eulerian-Eulerian two-phase model was developed to simulate the flow of carbon-based aqueous nanofluid in the direct absorption solar collector. The model included thermophoresis and optics of the sunlight absorption in the nanofluid. In the process, the two-fluid Eulerian-Eulerian

model simulated the transport of nanoparticles with the desired precision and at the moderate computational costs. The inter-particle collisions, which were not incorporated into the model, are of minor importance at the considered concentrations²². However, we do note that the model does not account for the particle-wall collisions, which might result in over-estimated absorbance at the walls.

The model was validated against the experimental data and furthermore used for the parametric optimization of the collector. The parameters considered were the concentration of the nanoparticles, the geometry of the collector, the flow rate and the absorptive properties of the boundaries.

The results of the CFD-analysis demonstrate asymmetry in the particulate phase concentration profile and the respective non-uniformity of the optical properties of the nanofluid. The deposition of the particles takes place in the collector so that a maximum 10% of the particles are captured in the DASC.

The model-based optimization resulted in 0.3 wt% optimum concentration of 30-nm nanoparticles and 300 μm thickness of the collector. The nanofluid velocity through the collector also has a significant impact on thermal efficiency. The maximum total efficiency of 87% is obtained when the flow velocity is 3 cm/s and decreases with higher velocities. The deposition efficiency and outlet temperature decrease for higher velocities.

The effect of the absorbing bottom surface of the collector was tested. The collector with a black bottom containing only water proved to be less effective than the collector with the volumetric absorption of the nanofluid. A top surface black absorber was also tested and was not shown to be efficient. However, the light-absorbing bottom boundary, when used together with the nanofluid, improves the thermal performance of the collector by a maximum of 12% for the cases when the channel size is under the optimum.

ACKNOWLEDGMENTS

This study was supported by the Russian Science Foundation (project No. 19-79-10083). The research mobility within the present collaboration is supported by the Norwegian Agency for International Cooperation (project UTF-2018-two-year/10036 TROIKA).

- ¹R. Saidur, K. Leong, and H. Mohammed, "A review on applications and challenges of nanofluids," *Renewable and Sustainable Energy Reviews* **15**, 1646–1668 (2011).
- ²D. A. Hagos, A. Gebremedhin, and B. Zethraeus, "Solar water heating as a potential source for inland norway energy mix," *Journal of Renewable Energy* **2014**, 968320 (2014).
- ³T. P. Otanicar, P. E. Phelan, R. S. Phrasher, G. Rosengarten, and R. A. Taylor, "Nanofluid-based direct absorption solar collector," *Journal of Renewable and Sustainable Energy* **2** (2010).
- ⁴M. Mirzaei, S. M. S. Hosseini, and A. M. M. Kashkooli, "Assessment of Al_2O_3 nanoparticles for the optimal operation of the flat plate solar collector," *Applied Thermal Engineering* **134**, 68 – 77 (2018).
- ⁵O. Neumann, A. S. Urban, J. Day, S. Lal, P. Nordlander, and N. J. Halas, "Solar vapor generation enabled by nanoparticles," *ACS Nano* **7**, 42–49 (2013).
- ⁶G. Ni, N. Miljkovic, H. Ghasemi, X. Huang, S. V. Borinska, C.-T. Lin, J. Wang, Y. Xu, M. M. Rahman, T. J. Zhang, and G. Chen, "Volumetric

solar heating of nanofluids for direct vapor generation," *Nano Energy* **17**, 290–301 (2015).

⁷H. Ghasemi, G. Ni, A. M. Marconnet, J. Loomis, S. Yerci, N. Miljkovic, and G. Chen, "Solar steam generation by heat localization," *Nature Communications* **5**, 4449 (2014).

⁸Z.-Q. Yin, X.-F. Li, F.-B. Bao, C.-X. Tu, and X. Y. Gao, "Thermophoresis and brownian motion effects on nanoparticle deposition inside a 90 degree square bend tube," *Aerosol and Air Quality Research* **18**, 1746–1756 (2018).

⁹Z. Haddad, E. Abu-Nada, H. F. Oztop, and A. Mataoui, "Natural convection in nanofluids: Are the thermophoresis and brownian motion effects significant in nanofluid heat transfer enhancement?" *International Journal of Thermal Sciences* **57**, 152 – 162 (2012).

¹⁰J. Burelbach, M. Zupkauskas, R. Lamboll, Y. Lan, and E. Eiser, "Colloidal motion under the action of a thermophoretic force," *The Journal of Chemical Physics* **147**, 094906 (2017).

¹¹O. Z. Sharaf, A. N. Al-Khateeb, D. C. Kyritsis, and E. Abu-Nada, "Direct absorption solar collector (dasc) modelling and simulation using a novel eulerian-lagrangian hybrid approach: Optical, thermal and hydrodynamic interactions," *Applied Energy* **231**, 1132–1145 (2018).

¹²O. Z. Sharaf, D. C. Kyritsis, A. N. Al-Khateeb, and E. Abu-Nada, "Effect of bottom surface optical boundary conditions on nanofluid-based dasc: Parametric study and optimization," *Solar Energy* **164**, 210 – 223 (2018).

¹³T. B. Gorji and A. A. Ranjbar, "Geometry optimization of a nanofluid-based direct absorption solar collector using response surface methodology," *Solar Energy* **122**, 314–325 (2015).

¹⁴B. V. Balakin and K. V. Kutsenko, "Magnetic enhancement of photothermal heating in ferrofluids," *Journal of Physics: Conference Series* **1133**, 012016 (2018).

¹⁵B. V. Balakin, O. V. Zhdaneev, A. Kosinska, and K. V. Kutsenko, "Direct absorption solar collector with magnetic nanofluid: Cfd model and parametric analysis," *Renewable Energy* **136**, 23 – 32 (2019).

¹⁶M. Lucas, P. Kosinski, and B. V. Balakin, "Eulerian-eulerian model for photothermal energy conversion in nanofluids," *AIP Conference Proceedings* **2116**, 030011 (2019).

¹⁷C. F. Bohren and D. R. Huffman, *Absorption and scattering of light by small particles* (Wiley, 1983).

¹⁸A. S. Hellesø, M. Ghaffari, B. V. Balakin, and A. C. Hoffmann, "A parametric study of cohesive particle agglomeration on a shear flow - numerical simulations by the discrete element method," *Journal of Dispersion Science and Technology* **38** - 5, 611–620 (2017).

¹⁹W. Wagner and A. Prüb, "The iapws formulation 1995 for the thermodynamic properties of ordinary water substance for general and scientific use," *Journal of Physical and Chemical Reference Data* **31**, 387–535 (2002).

²⁰S. P. S. Simcenter, "Star-ccm+ user guide for version 13.06," (2019).

²¹F. Duan, T. F. Wong, and A. Crivoi, "Dynamic viscosity measurement in non-newtonian graphite nanofluids," *Nanoscale Research Letters* **7**, 36 (2012).

²²C. T. Crowe, J. D. Schwartzkopf, M. Sommerfeld, and Y. Tsuji, *Multiphase flows with droplets and particles* (CRC press, 2012).

²³J. R. Brock, "On the theory of thermal forces acting on aerosol particles," *Journal of Colloid Science* **17**, 768–780 (1962).

²⁴M. Kalteh, A. Abbassi, M. Saffar-Aval, and J. Harting, "Eulerian-eulerian two-phase numerical simulation of nanofluid laminar forced convection in a microchannel," *International Journal of Heat and Fluid Flow* **32**, 107–116 (2011).

²⁵S. K. Hota and G. Diaz, "Activated carbon dispersion as absorber for solar water evaporation: A parametric analysis," *Solar Energy* **184**, 40 – 51 (2019).

²⁶R. A. Taylor, P. E. Phelan, T. P. Ottanar, R. Adrian, and R. Prasher, "Nanofluid optical property characterization: towards efficient direct absorption solar collectors," *Nanoscale Research Letters* **6**, 225 (2011).

²⁷G. M. Hale and M. R. Querry, "Optical constants of water in the 200-nm to 200- μ m wavelength region," *Applied Optics* **12**, 555–563 (1973).

²⁸H. Phillip and E. Taft, "Kramers-kronig analysis of reflectance data for diamond," *Physical Review* **136**, A1445–A1448 (1964).

²⁹R. Bird, R. Hulstrom, and L. Lewis, "Terrestrial solar spectral data sets," *Solar Energy* **30**, 563 – 573 (1983).

³⁰C. A. Gueymard, D. Myers, and K. Emery, "Proposed reference irradiance spectra for solar energy systems testing," *Solar Energy* **73**, 443–467 (2002).

³¹C. A. Gueymard, "The sun's total and spectral irradiance for solar energy applications and solar radiation models," *Solar Energy* **76**, 423 – 453 (2004).

³²L. M. Adams and J. L. Nazareth, "Linear and nonlinear conjugate gradient-related methods," in *Proceedings in Applied Mathematics Ser. Vol. 85* (1996).

³³ASHRAE, "ANSI/ASHRAE 93-1986 (RA 91). Methods of testing to determine the thermal performance of solar collectors," (1991).

³⁴J. D. Anderson, *Computational Fluid Dynamics, The Basics with Applications* (McGraw-Hill Education, 1995).

³⁵B. E. Rapp, *Microfluids: Modelling, Mechanics and Mathematics* (Elsevier, 2017).

³⁶W. L. McCabe, J. C. Smith, and P. Harriot, *Unit Operations of Chemical Engineering* (McGraw-Hill, 2005).

³⁷O. Ibe, *Markov Processes for Stochastic Modelling* (Elsevier, 2013).

³⁸R. Baierlein, *Thermal Physics* (The University of Cambridge, 1999).

³⁹Y. A. Cengel and M. A. Boles, *Thermodynamics - An Engineering Approach* (McGraw-Hill, 1994).

⁴⁰P. Atkins and J. de Paula, *Physical Chemistry* (Oxford University Press, 2014).

⁴¹R. M. Mazo, *Brownian Motion: Fluctuations, Dynamics and Applications* (Oxford University Press, 2002).

⁴²D.-Y. Shang and L.-C. Zhong, *Heat Transfer Due to Laminar Natural Convection of Nanofluids* (Springer, 2019).

⁴³Z. Warhaft, *The Engine and the Atmosphere: An Introduction to Engineering* (Cambridge University Press, 1997).

⁴⁴D. C. Wilcox, *Turbulence Modeling for CFD* (DCW Industries, 2006).

⁴⁵W. Graebel, *Advanced Fluid Mechanics* (Elsevier Science, 2007).

⁴⁶J. H. Lienhard, *A Heat Transfer Textbook* (Phlogiston Press, 2019).

⁴⁷J. Philip and P. Shima, "Thermal properties of nanofluids," *Advances in Colloid and Interface Science* **183–184**, 30–45 (2012).

⁴⁸Z. Valizadeh and M. Shams, "Numerical investigation of water-based nanofluid subcooled flow boiling by three-phase euler-euler, euler-lagrange approach," *Heat Mass Transfer* **52**, 1501–1514 (2015).

⁴⁹S. Dong, L. Zheng, X. Zhang, S. Wu, and B. Shen, "A new model for brownian force and the application to simulating nanofluid flow," *Microfluidics and Nanofluidics* (2013).

⁵⁰M. Abarham, P. Zamankhan, J. W. Hoard, D. Styles, C. S. Sluder, J. M. E. Storey, M. J. Lance, and D. Assanis, "Cfd analysis of particle transport in axi-symmetric tube flows under the influence of thermophoretic force," *International Journal of Heat and Mass Transfer* **61**, 94–105 (2013).

⁵¹B. Wang, X. Wang, W. Lou, and J. Hao, "Thermal conductivity and rheological properties of graphite/oil nanofluids," *Colloids and Surfaces A: Physicochemical and Engineering Aspects* **414**, 125–131 (2012).

⁵²A. Kamyar, R. Saidur, and M. Hasanuzzaman, "Application of computational fluid dynamics (cfd) for nanofluids," *International Journal of Heat and Mass Transfer* **55**, 4104–4115 (2012).

⁵³J. Liu, Z. Ye, L. Zhang, X. Fang, and Z. Zhang, "A combined numerical and experimental study on graphene/ionic liquid nanofluid based on direct absorption solar collector," *Solar Energy Materials and solar Cells* **136**, 177–186 (2015).

⁵⁴S. J. Palm, G. Roy, and C. T. Nguyen, "Heat transfer enhancement with the use of nanofluids in radial flow cooling systems considering temperature dependent properties," *Applied Thermal Engineering* **26**, 2209–2218 (2006).

⁵⁵Y. Ding and D. Wen, "Particle migration in a flow of nanoparticle suspensions," *Powder Technology* **149**, 84–92 (2005).

⁵⁶J.-H. Lee, K. S. Hwang, S. P. Jang, B. H. Lee, J. H. Kim, S. U. Choi, and C. J. Choi, "Effective viscosities and thermal conductivities of aqueous nanofluids containing low volume concentrations of Al_2O_3 nanoparticles," *International Journal of Heat and Mass Transfer* **51**, 2651–2656 (2008).

⁵⁷D. Han, Z. Meng, D. Wu, C. Zhang, and H. Zhu, "Thermal properties of carbon black aqueous nanofluids for solar absorption," *Nanoscale Research Letters* **6**, 457 (2011).

⁵⁸E. Bellos, Z. Sais, and C. Tzivanidis, "The use of nanofluids in solar concentrating technologies: A comprehensive review," *Journal of Cleaner Production* **196**, 84–99 (2018).

⁵⁹A. Elseikh, S. Sharshir, M. E. Mostafa, F. Essa, and M. K. A. Ali, "Applications of nanofluids in solar energy: A review of recent advances," *Re-*

This is the author's peer reviewed, accepted manuscript. However, the online version of record will be different from this version once it has been copyedited and typeset.

PLEASE CITE THIS ARTICLE AS DOI: 10.1063/1.5144737

Sample title

8

- newable and Sustainable Energy Reviews (2017).
- ⁶¹V. Rastegar, G. Ahmadi, and S. Babu, "Filtration of aqueous colloidal ceria slurries using fibrous filters - an experimental and simulation study," *Separation and Purification Technology* **176**, 231–242 (2017).
- ⁶²Z. Luo, C. Wang, W. Wei, G. Xiao, and M. Ni, "Performance improvement of a nanofluid solar collector based on direct absorption collection (dac) concepts," *International Journal of Heat and Mass Transfer* **75**, 262–278 (2014).
- ⁶³H. Jin, G. Lin, L. Bai, M. Amjad, E. P. B. Filho, and D. Wen, "Photothermal conversion efficiency of nanofluids: An experimental and numerical study," *Solar Energy* **139**, 278–289 (2016).
- ⁶⁴M. Karami, M. A. Akhavan-Bahabadi, S. Delfini, and M. Raisee, "Experimental investigation of a nanofluid-based direct absorption solar collector for residential applications," *Renewable and Sustainable Energy Reviews* **52**, 793–801 (2015).
- ⁶⁵R. Saidur, T. Meng, M. Hasanuzzaman, and A. Kamyar, "Evaluation of the effect of nanofluid-based absorbers on direct solar collector," *International Journal of Heat and Mass Transfer* **55**, 5899–5909 (2012).
- ⁶⁶E. T. Ulset, P. Kosinski, Y. Zabeednova, O. V. Zhdanov, P. G. Struchalin, and B. V. Balakin, "Photothermal boiling in aqueous nanofluids," *Nano Energy* **50**, 339–346 (2018).
- ⁶⁷S. Rashid, J. A. Esfahani, and R. Ellahi, "Convective heat transfer and particle motion in an obstructed duct with two side by side obstacles by means of dpm model," *Applied Sciences* **7**, 431–445 (2017).
- ⁶⁸J. E. Minardi and H. N. Chuang, "Performance of a black liquid flat-plate solar collector," *Solar Energy* **17**, 179–183 (1975).
- ⁶⁹K. Zhukovsky, D. Oskolkov, and N. Gubina, "Some exact solutions to non-fourier heat equations with substantial derivative," *Axioms* **7**, 179–183 (2018).
- ⁷⁰Z. Fang, Y.-R. Zhen, O. Neumann, A. Polman, F. J. G. de Abajo, P. Nordlander, and N. J. Halas, "Evolution of light-induced vapor generation at a liquid-immersed metallic nanoparticle," *NANO Letters* **13**, 1736–1742 (2013).
- ⁷¹N. Lebovka, S. Khrapaty, R. Melnyk, and M. Vygnomitskii, "Effects of hydrodynamic retardation and interparticle interactions on the self-assembly in a drying droplet containing suspended solid particles," *Physical Review* **89** (2014).
- ⁷²L. Zhang, J. Shao, and X. Chen, "Cfd simulation of nozzle characteristics in a gas aggregation cluster source," *Vacuum* **129**, 105–110 (2016).
- ⁷³T. Shekhalipour and A. Abbassi, "Numerical analysis of nanofluid flow inside a trapezoidal microchannel using different approaches," *Advanced Powder Technology* **29**, 1749–1757 (2018).
- ⁷⁴M. H. Fard, M. N. Esfahani, and M. Talaie, "Numerical study of convective heat transfer of nanofluids in a circular tube two-phase model versus single model," *International Communications in Heat and Mass Transfer* **37**, 91–97 (2010).
- ⁷⁵N. Akram, R. Sadri, S. Kazi, M. N. M. Zubir, M. Ridha, W. Ahmed, M. E. M. Soudagar, and M. Arzpeyma, "A comprehensive review on nanofluid operated solar flat plate collectors," *Journal of Thermal Analysis and Calorimetry* (2019).
- ⁷⁶O. Mahian, A. Kianifar, S. A. Kalogirou, I. Pop, and S. Wongwises, "A review of the applications of nanofluids in solar energy," *International Journal of Heat and Mass Transfer* **57**, 582–594 (2013).
- ⁷⁷D. Wen, L. Zhang, and Y. He, "Flow and migration of nanoparticle in a single channel," *Heat Mass Transfer* **45**, 1061–1067 (2009).
- ⁷⁸K. M. Pandey and R. Chaurasiya, "A review on analysis and development of solar flat plate collector," *Renewable and Sustainable Energy Reviews* **67**, 641–650 (2017).
- ⁷⁹W. M. Hashim, A. T. Shomran, H. A. Jurmut, T. S. Gaaz, A. A. H. Kadhum, and A. A. Al-Amiery, "Case study on solar water heating for flat plate collector," *Case studies in Thermal Engineering* **12**, 666–671 (2018).
- ⁸⁰H. Bhowmik and R. Amin, "Efficiency improvement of flat plate solar collectors using reflector," *Energy Reports* **3**, 119–123 (2017).
- ⁸¹F. Roelofs and A. Shams, "Cfd - introduction," *Thermal Hydraulics Aspects of Liquid Metal Cooled Nuclear Reactors*, 213–218 (2019).
- ⁸²N. J. Hogan, A. S. Urban, C. Ayala-Orozco, A. Pimpinelli, P. Nordlander, and N. J. Halas, "Nanoparticles heat through light localization," *Nano Letters* **14**, 4640–4645 (2014).
- ⁸³A. M. Helmenstine, "An introduction to brownian motion," (2019), last accessed 28 June 2019.
- ⁸⁴"What is cfd, computational fluid dynamics?" (2017), last accessed 01 July 2019.
- ⁸⁵B. Pedersen, "Termodynamikk," (2018), last accessed 16 August 2019.
- ⁸⁶E. S. Egeland, "Beer's lov," (2017), last accessed 26 August 2019.
- ⁸⁷D. A. Verma, "National programme on technology enhanced learning; heat transfer," (2012), last accessed 19 August 2019.
- ⁸⁸E. ToolBox, "Water - heat capacity (specific heat)," (2004), last accessed 27 August 2019.
- ⁸⁹R. G. Newell, D. Raimi, and G. Aldana, "Global energy outlook 2019: The next generation of energy," (2019), last accessed 28 August 2019.
- ⁹⁰E. Toolbox, "Water - dynamic and kinematic viscosity," (2004), last accessed 11 September 2019.
- ⁹¹C. F. Boren and D. R. Huffman, "Absorption and scattering by a sphere," in *Absorption and Scattering of Light by Small Particles* (John Wiley and Sons, Ltd, 2007) Chap. 4, pp. 82–129, <https://onlinelibrary.wiley.com/doi/pdf/10.1002/9783527618156.ch4>.
- ⁹²C. F. Boren and D. R. Huffman, "Particles small compared with the wavelength," in *Absorption and Scattering of Light by Small Particles* (John Wiley and Sons, Ltd, 2007) Chap. 5, pp. 130–157, <https://onlinelibrary.wiley.com/doi/pdf/10.1002/9783527618156.ch5>.
- ⁹³Y. Su, D. D. Chen, L. Gong, and B. Li, "Thermal and physical properties of graphite water-based nanofluids used in minimum quantity lubrication," in *2014 International Conference on Mechatronics, Electronic, Industrial and Control Engineering (MEIC-14)* (Atlantis Press, 2014).

This is the author's peer reviewed, accepted manuscript. However, the online version of record will be different from this version once it has been copyedited and typeset.

PLEASE CITE THIS ARTICLE AS DOI: 10.1063/1.5144737

Sample title

9

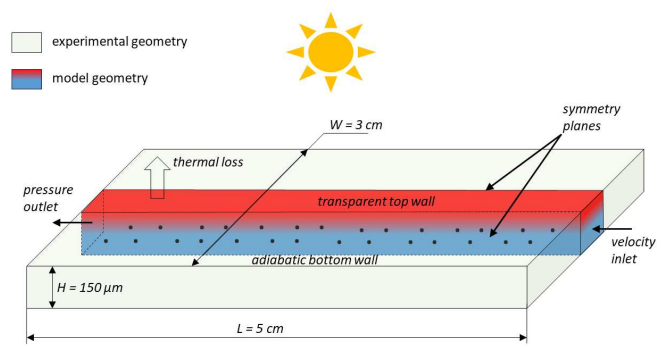


FIG. 1. Schematic description of the model and the experiment.

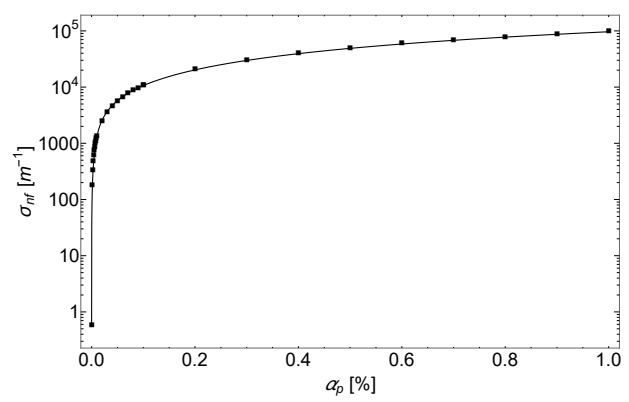


FIG. 2. Equivalent extinction coefficient as a function of particle concentration.

Sample title

10

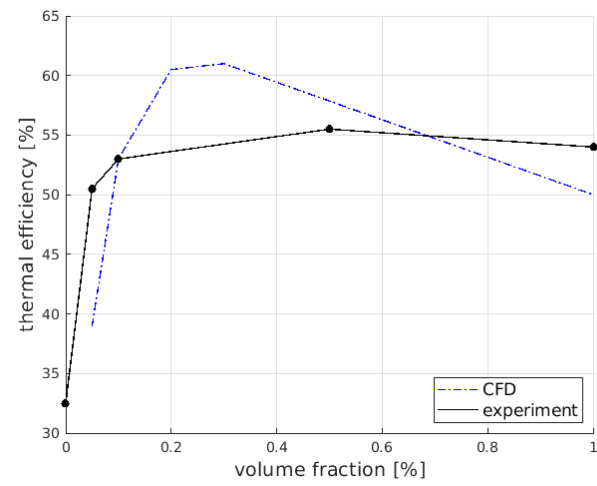


FIG. 3. Thermal efficiency as a function of particle concentration

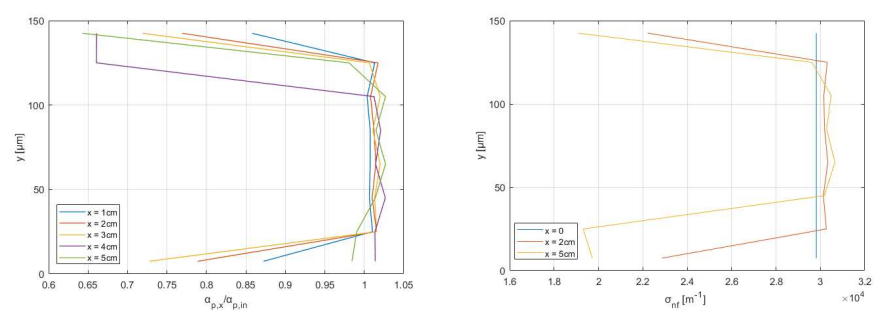


FIG. 4. a) Transverse distribution of particle concentration, scaled by the inlet value and b) the nanofluid extinction coefficient at different axial coordinates of the collector.

Sample title

11

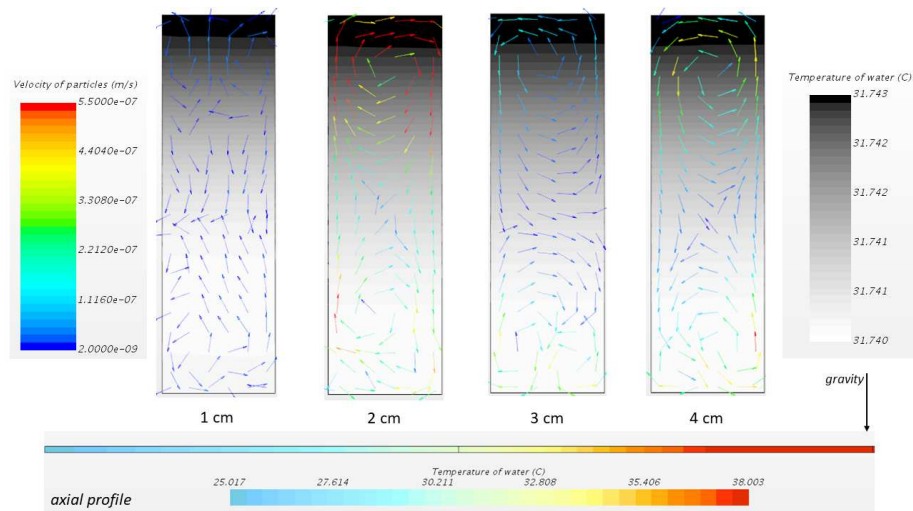


FIG. 5. Contours of the fluid phase temperature together with the particle velocity vectors in the orthogonal cross sections at 1 cm, 2 cm, 3 cm, 4 cm from the inlet. The insert at the bottom presents the axial distribution of temperature in DASC. The particle concentration is 0.5%.

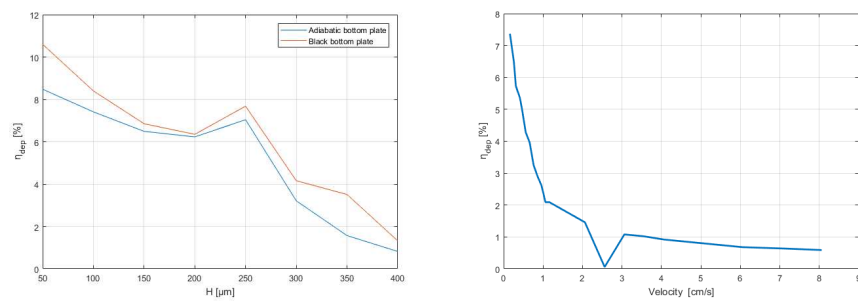


FIG. 6. Deposition efficiency as a function of a) collector height and b) inlet velocity.

This is the author's peer reviewed, accepted manuscript. However, the online version of record will be different from this version once it has been copyedited and typeset.

PLEASE CITE THIS ARTICLE AS DOI: 10.1063/1.5144737

Sample title

12

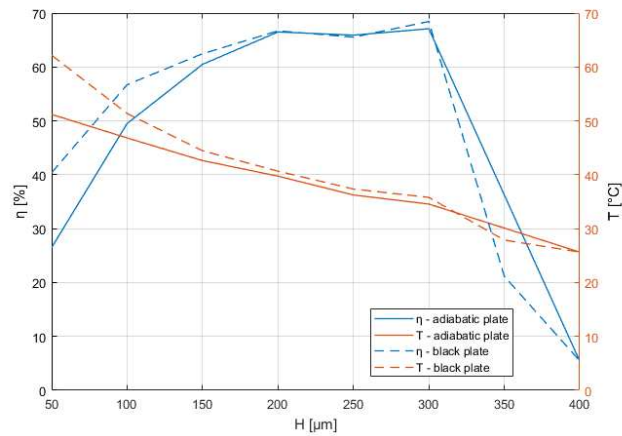


FIG. 7. Thermal efficiency and outlet temperature as a function of collector height for different types of boundary conditions at 0.3 wt% NPs and 0.26 cm/s fluid velocity.

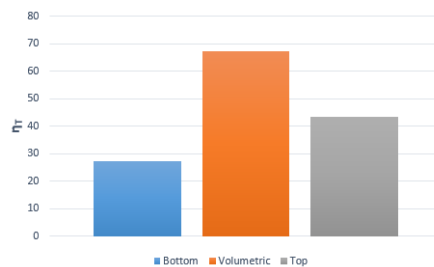


FIG. 8. Thermal efficiency for different types of boundary conditions.

This is the author's peer reviewed, accepted manuscript. However, the online version of record will be different from this version once it has been copyedited and typeset.

PLEASE CITE THIS ARTICLE AS DOI: 10.1063/1.5144737

Sample title

13

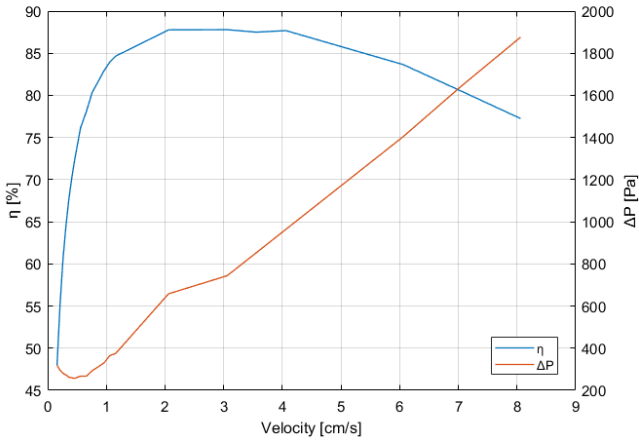
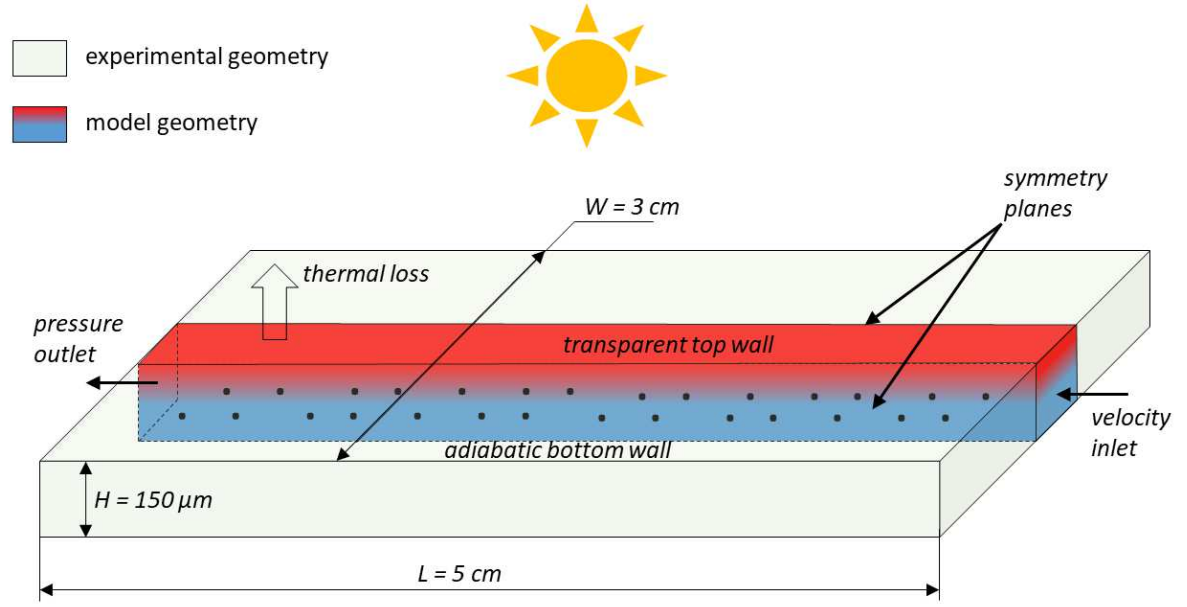


FIG. 9. Total efficiency and pressure loss as a function of nanofluid velocity.

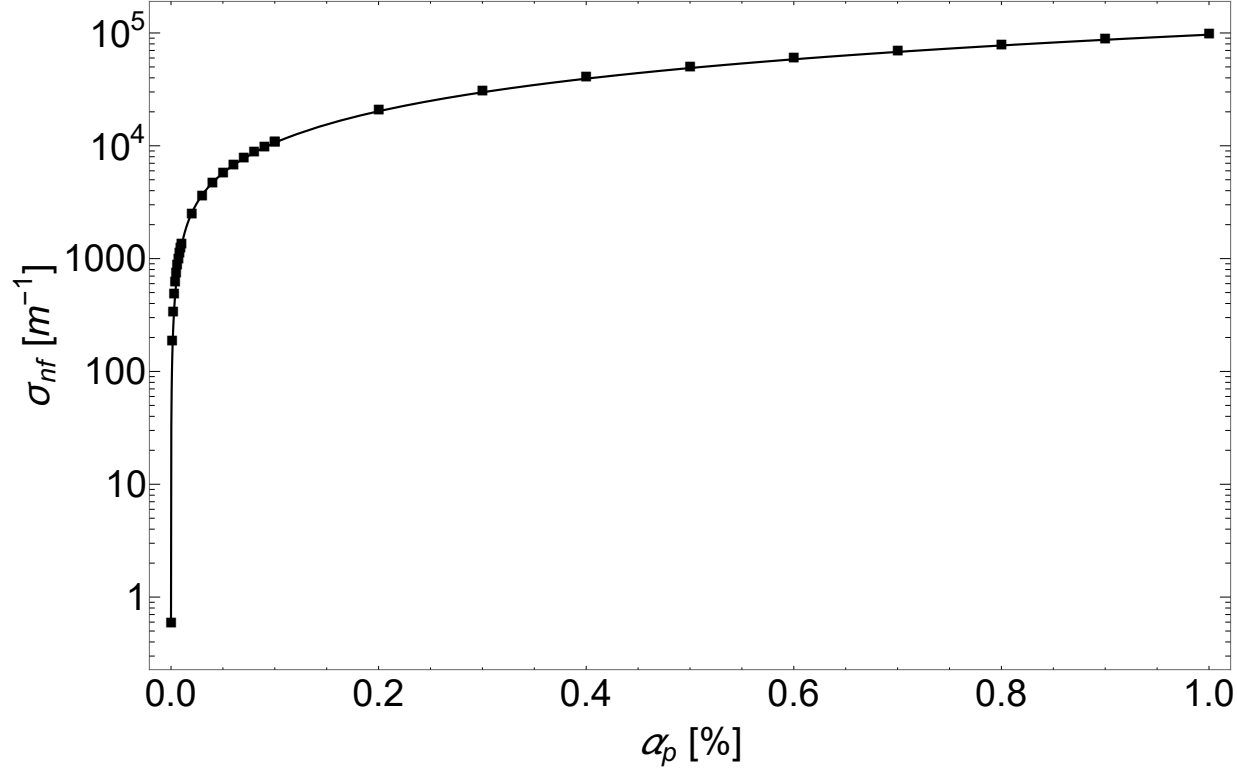
This is the author's peer reviewed, accepted manuscript. However, the online version of record will be different from this version once it has been copyedited and typeset.

PLEASE CITE THIS ARTICLE AS DOI: 10.1063/1.5144737



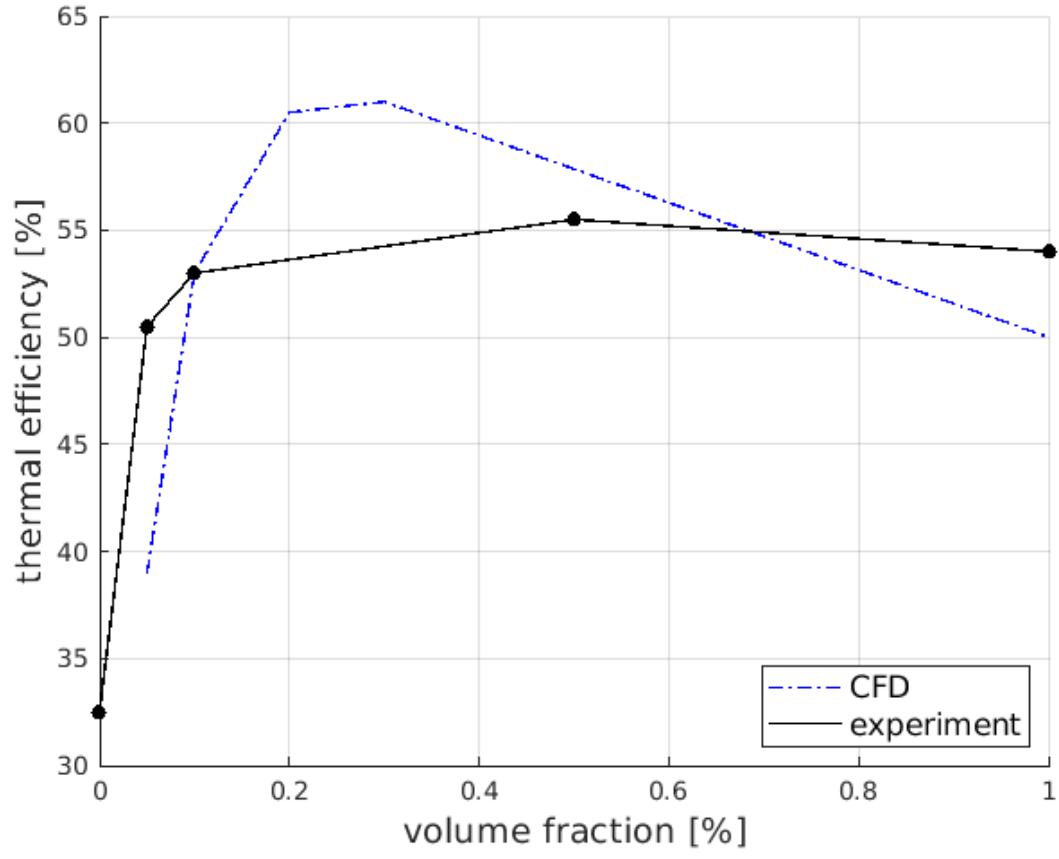
This is the author's peer reviewed, accepted manuscript. However, the online version of record will be different from this version once it has been copyedited and typeset.

PLEASE CITE THIS ARTICLE AS DOI: 10.1063/1.5144737



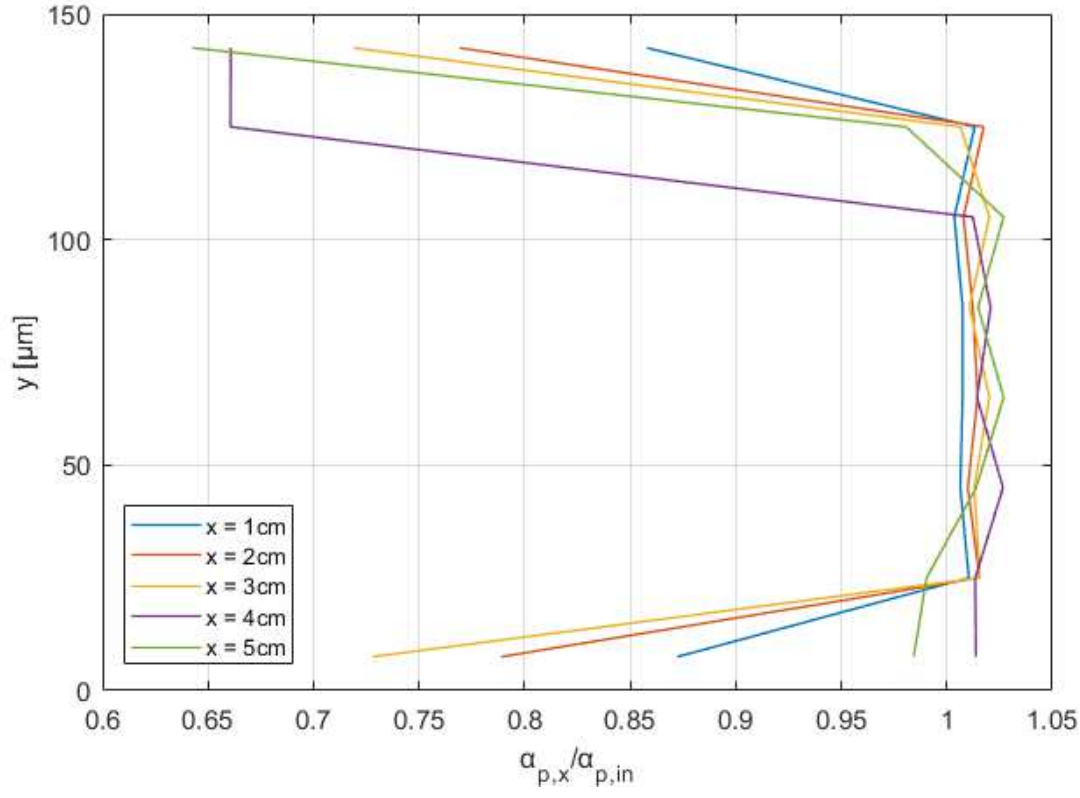
This is the author's peer reviewed, accepted manuscript. However, the online version of record will be different from this version once it has been copyedited and typeset.

PLEASE CITE THIS ARTICLE AS DOI: 10.1063/1.5144737



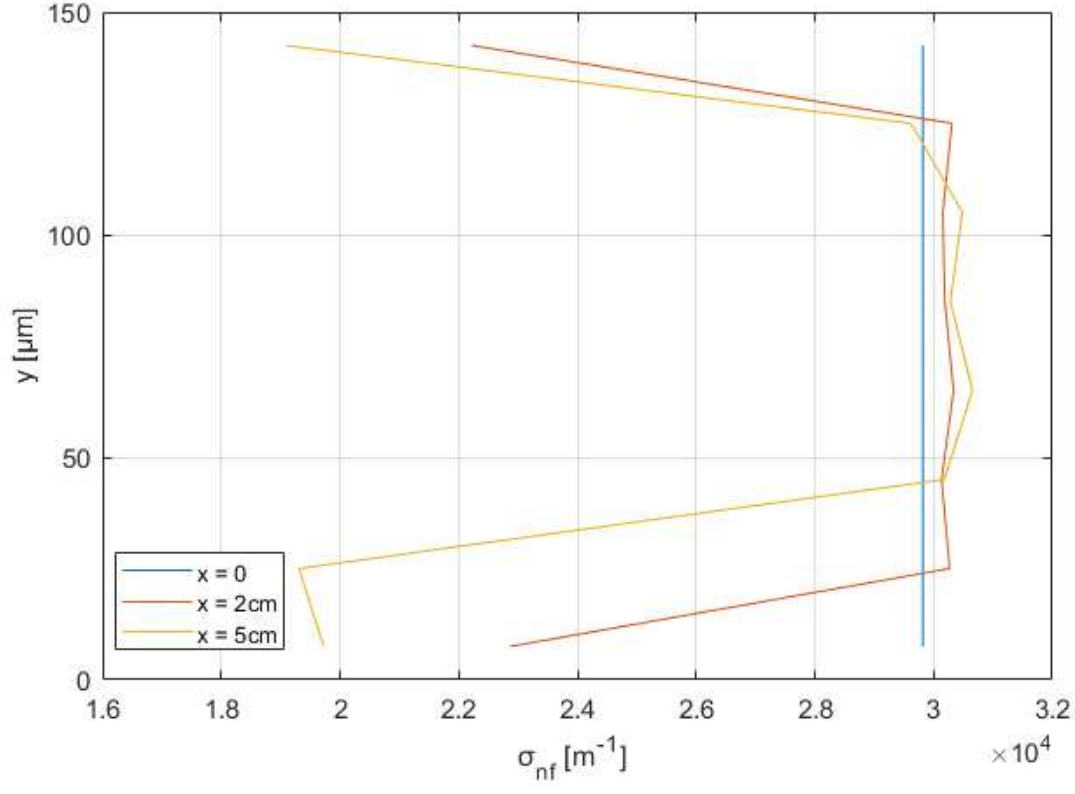
This is the author's peer reviewed, accepted manuscript. However, the online version of record will be different from this version once it has been copyedited and typeset.

PLEASE CITE THIS ARTICLE AS DOI: 10.1063/1.5144737



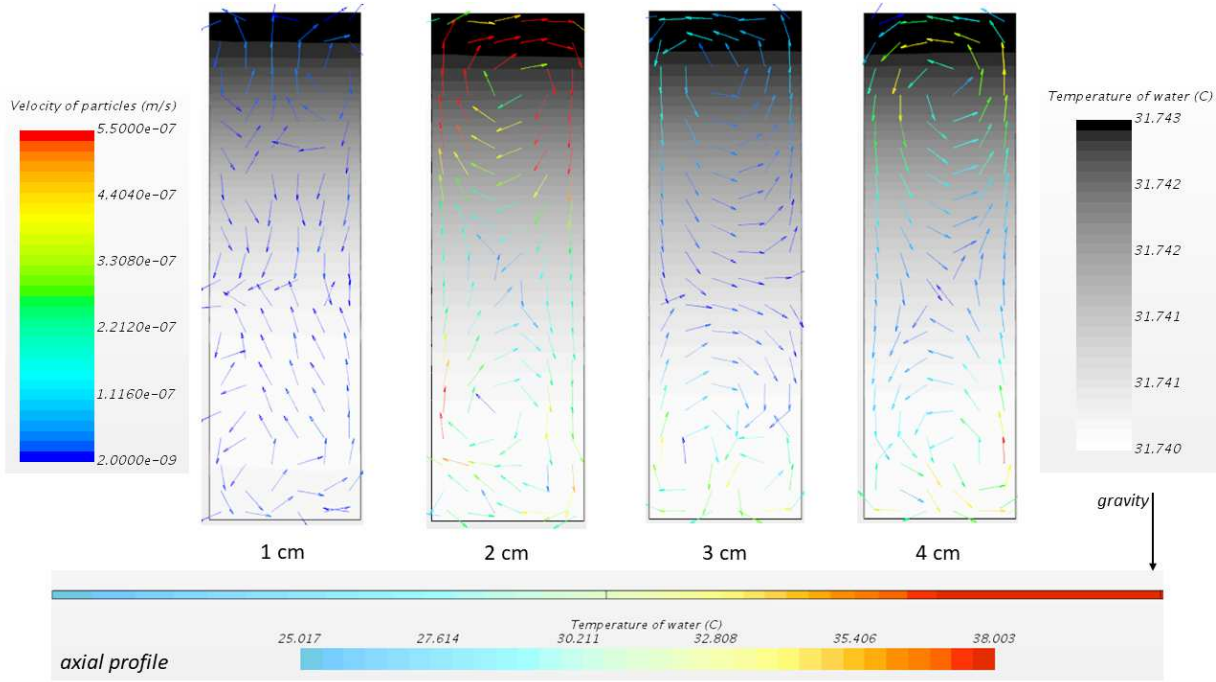
This is the author's peer reviewed, accepted manuscript. However, the online version of record will be different from this version once it has been copyedited and typeset.

PLEASE CITE THIS ARTICLE AS DOI: 10.1063/1.5144737



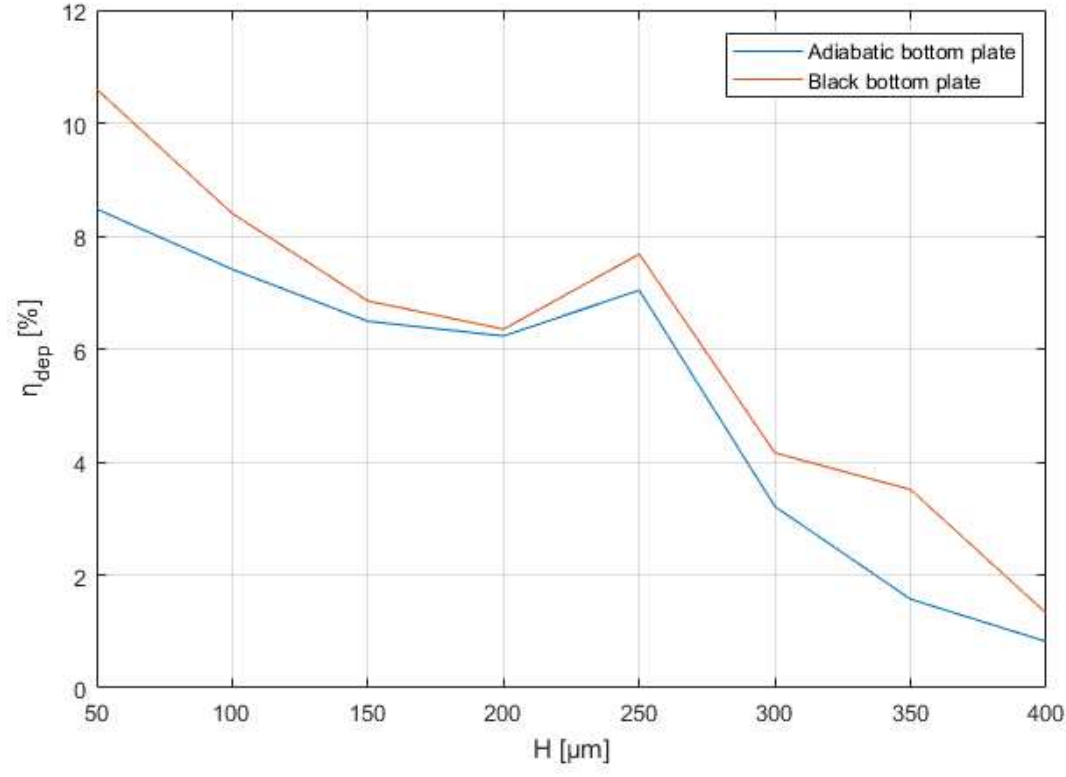
This is the author's peer reviewed, accepted manuscript. However, the online version of record will be different from this version once it has been copyedited and typeset.

PLEASE CITE THIS ARTICLE AS DOI: 10.1063/1.5144737



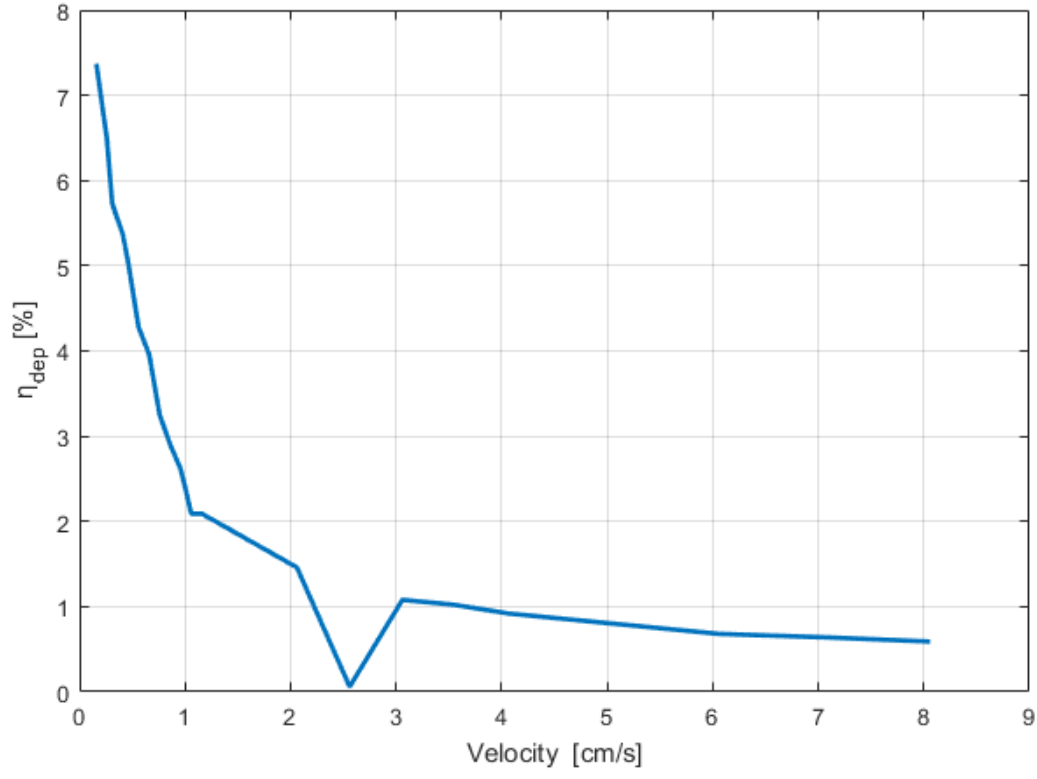
This is the author's peer reviewed, accepted manuscript. However, the online version of record will be different from this version once it has been copyedited and typeset.

PLEASE CITE THIS ARTICLE AS DOI: 10.1063/1.5144737



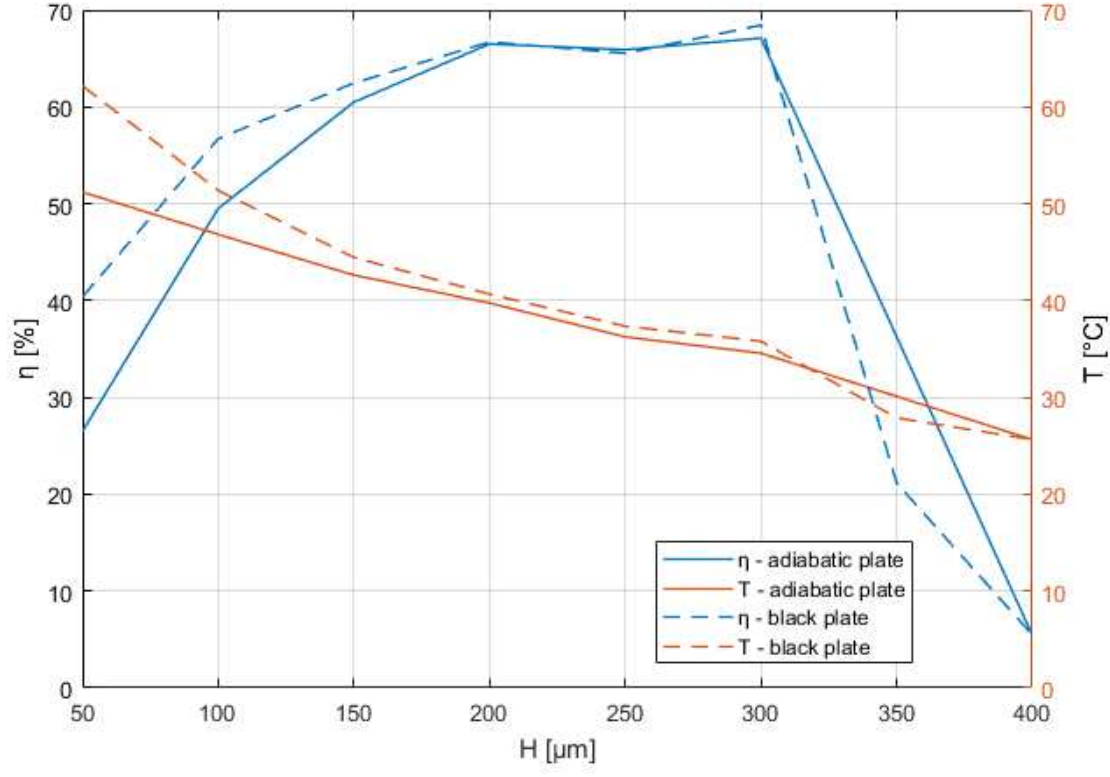
This is the author's peer reviewed, accepted manuscript. However, the online version of record will be different from this version once it has been copyedited and typeset.

PLEASE CITE THIS ARTICLE AS DOI: 10.1063/1.5144737



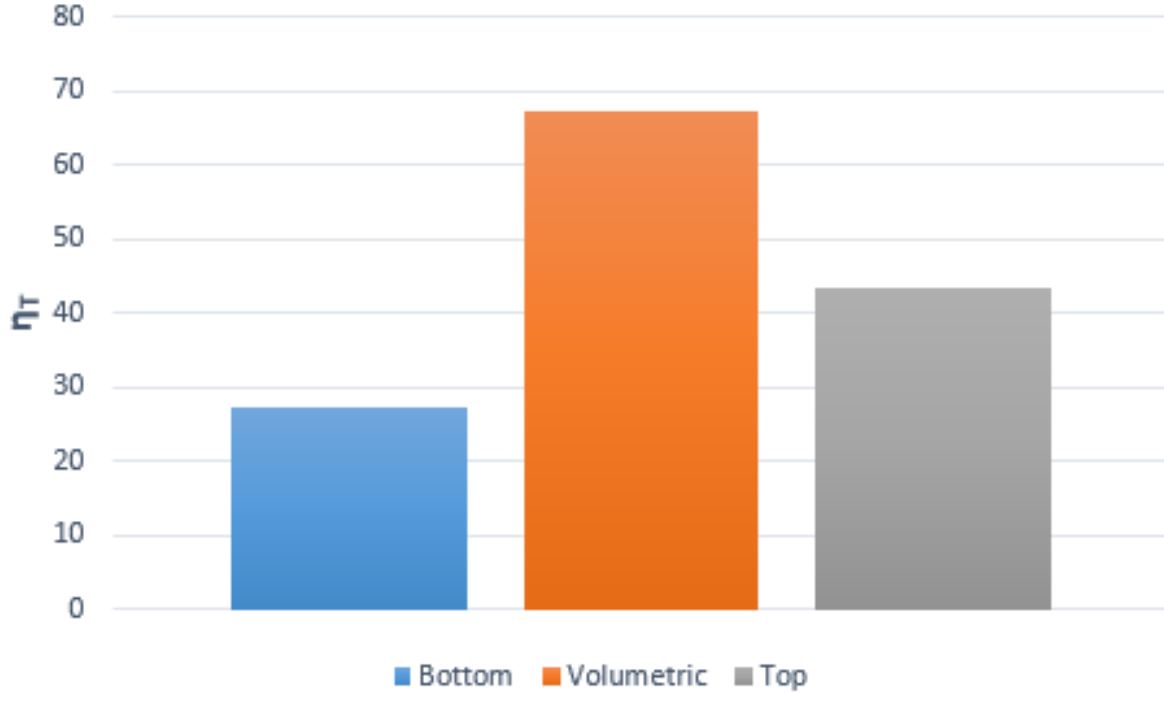
This is the author's peer reviewed, accepted manuscript. However, the online version of record will be different from this version once it has been copyedited and typeset.

PLEASE CITE THIS ARTICLE AS DOI: 10.1063/1.5144737



This is the author's peer reviewed, accepted manuscript. However, the online version of record will be different from this version once it has been copyedited and typeset.

PLEASE CITE THIS ARTICLE AS DOI: 10.1063/1.5144737



This is the author's peer reviewed, accepted manuscript. However, the online version of record will be different from this version once it has been copyedited and typeset.

PLEASE CITE THIS ARTICLE AS DOI: 10.1063/1.5144737

